ADVANCED FUNCTIONAL MATERIALS
www.afm-journal.de

Nickel Hydroxide-Supported Ru Single Atoms and Pd Nanoclusters for Enhanced Electrocatalytic Hydrogen Evolution and Ethanol Oxidation

An Pei, Guang Li, Lihua Zhu, Zinan Huang, Jinyu Ye, Yu-Chung Chang, Sameh M. Osman, Chih-Wen Pao, Qingsheng Gao, Bing Hui Chen, and Rafael Luque**

The rational fabrication of Pt-free catalysts for driving the development of practical applications in alkaline water electrolysis and fuel cells is promising but challenging. Herein, a promising approach is outlined for the rational design of multimetallic catalysts comprising multiple active sites including Pd nanoclusters and Ru single atoms anchored at the defective sites of $Ni(OH)_2$ to simultaneously enhance hydrogen evolution reactions (HER) and ethanol oxidation reactions (EOR). Remarkably, $Pd_{12}Ru_3/Ni(OH)_2/C$ exhibits a remarkably reduced HER overpotential (16.1 mV@10 mA cm^{-2} with a Tafel slope of 21.8 mV dec^{-1}) as compared to commercial 20 wt.% Pt/C (26.0 mV@10 mA cm^{-2}, 32.5 mV dec^{-1}). More importantly, $Pd_{12}Ru_3/Ni(OH)_2/C$ possesses a self-optimized overpotential to 12.5 mV@10 mA cm^{-2} after 20 000 cycles stability test while a significantly decreased performance for commercial 20wt.% Pt/C (64.5 mV@10 mA cm^{-2} after 5000 cycles). The mass activity of $Pd_{12}Ru_3/Ni(OH)_2/C$ for the EOR is up to 3.724 A mg_{PdRu}^{-1}, ≈20 times higher than that of commercial Pd/C. Electrochemical in situ Fourier transform infrared measurements confirm the enhanced CO_2 selectivity of $Pd_{12}Ru_3/Ni(OH)_2/C$ while synergistic and electronic effects of adjacent Ru, Pd, and OH_{ad} adsorption on $Ni(OH)_2$ at low potential play a key role during EOR.

1. Introduction

The advantage of appropriately combining hydrogen energy with fuel cells has attracted significant attention worldwide due to the ever-growing exhausted fossil energy and environmental pollution.[1–3] Hydrogen energy is emerging as an effective carbon neutrality alternative to traditional fossil fuels due to its renewable and zero-emission nature.[4,5] Renewable energy, especially intermittent energy such as wind power,[6] solar power,[7] and tidal power[8] can be stably stored in hydrogen via water electrolysis. Such energy conversion into hydrogen as an energy storage form can perfectly solve the problem of energy loss due to the self-discharge of energy storage devices.[9,10] To date, despite the existence of various pathways for hydrogen production, alkaline water electrolysis features unique advantages including unlimited reactant availability, good manufacturing safety, stable

A. Pei, L. Zhu
Jiangxi Provincial Key Laboratory of Functional Molecular Materials Chemistry
College of Chemistry and Chemical Engineering
Faculty of Materials Metallurgy and Chemistry
Jiangxi University of Science and Technology
Ganzhou, Jiang Xi 341000, China
E-mail: lihuazhu@stu.xmu.edu.cn

G. Li, J. Ye, B. H. Chen
College of Chemistry and Chemical Engineering
Xiamen University
Xiamen 361005, China

The ORCID identification number(s) for the author(s) of this article can be found under https://doi.org/10.1002/adfm.202208587.

DOI: 10.1002/adfm.202208587

Z. Huang, Q. Gao
College of Chemistry and Materials Science
and Guangdong Provincial Key Laboratory of Functional Supramolecular Coordination Materials and Applications
Jinan University
Guangzhou 510632, China

Y.-C. Chang, C.-W. Pao
National Synchrotron Radiation Research Center
Hsinchu 300, Taiwan

S. M. Osman
Chemistry Department
College of Science
King Saud University
P.O. Box 2455, Riyadh 11451, Saudi Arabia

R. Luque
Departamento de Química Orgánica
Universidad de Córdoba
Campus de Rabanales, Edificio Marie Curie (C-3), Ctra Nnal IV, Km 396, E14071 Córdoba, Spain
E-mail: q62alsor@uco.es

R. Luque
Peoples Friendship University of Russia (RUDN University)
6 Miklukho Maklaya str., Moscow 117198, Russian Federation

output, and high product purity.[11,12] Renewable energy conversion devices of direct ethanol fuel cells (DEFCs) have also emerged with uniquely relevant advantages (e.g., safe storage, portable, high-energy density, and security).[13–16] The development of ethanol oxidation reactions (EOR) in alkaline conditions is of critical importance for the commercial viability of DEFCs technology.[17]

In this regard, the rational fabrication of effective and durable bifunctional electrocatalysts for the HER and EOR in an alkaline medium is significant for the development of renewable energy storage and conversion devices.[12,13] However, traditional Pt-based catalysts suffer from both sluggish kinetics of the HER and CO_{ad} easy-poisoning during EOR under alkaline conditions.[18,19] Besides, the high price and scarcity of Pt are still significant obstacles to the enhancement of high-efficiency fuel cells.[20] The oxyphilic metal of ruthenium (Ru) is recognized as a relevant alternative to Pt for efficient HER because it can lower the reaction barrier of the rate-determining step by weakening the hydrogen-binding energy and promoting OH adsorption during HER.[21–23] Qin and co-workers[21] synthesized the Pd_3Ru alloy catalysts with Ru single atoms and clusters being segregated on the surface, Pd_3Ru alloy dramatically lowered the overpotential to 104 mV at 10 mA cm^{-2} toward the HER relative to Pd/C. Additionally, transition metal hydroxides are considered to reduce overpotentials in HER.[24,25] For example, Subbaraman[26] et al. developed well-characterized $M^{2+\delta}O^{\delta}(OH)_{2-\delta}$/Pt(111) catalyst surfaces (M = Ni, Co, Fe, and Mn) and established a descriptor (OH_{ad}-$M^{2+\delta}$) to conclude that water-dissociation reactivity was Mn < Fe < Co < Ni. Transition metal hydroxides (e.g., $Ni(OH)_2$) were also demonstrated to promote CO oxidation in alcohol oxidation.[27,28] As for the Pt-free catalysts, palladium (Pd) was proved to own remarkable electrocatalytic activity and CO-tolerance stability, especially the excellent intrinsic oxidation property toward C—C bond cleavage.[29,30] The relatively low cost of the Pd-based electrocatalysts also makes them promising alternatives to the Pt-based electrocatalysts for alkaline EOR.[31] To date, significant scientific efforts have been devoted to designing a facile yet efficient experimental section for the construction of the Pd-based electrocatalysts with enhanced HER and EOR electrocatalytic performance.[32–34] For instance, Gao's group[35] developed a universal route for the precise synthesis of self-standing Pd-M (M = Ag, Pb, Au, Ga, Cu, and Pt, etc.), and the Pd-M systems exhibited enhanced EOR mass activity and stability as compared to commercial Pd/C.

In view of previous works in our group on the regulation of precious metals and hydroxides,[36,37] the rational combination of Pd, Ru, and transition metal hydroxides species may provide a promising strategy for the design of advanced functional electrocatalysts with outstanding activity and favorable toxicity resistance. Herein, we report a universal method for the rational design of $Pd_xRu_y/Ni(OH)_2/C$ with different Pd/Ru ratios (x:y is the atomic ratio) with Pd nanoclusters, Ru single atoms anchored at the defective sites of $Ni(OH)_2$ for accelerating HER and EOR reactivity in alkaline medium. Impressively, the coordination parameters and detailed nanostructures of $Pd_{12}Ru_3/Ni(OH)_2/C$ could be revealed by X-ray absorption spectroscopy (XAS), aberration-corrected scanning transmission electron microscope (AC-STEM), and other techniques. The mechanism of the structure-activity relationship during highly efficient HER and EOR processes over $Pd_{12}Ru_3/Ni(OH)_2/C$ was further determined by conducting electrochemical in situ Raman spectroscopy and in situ infrared spectroscopy, respectively. This work could pave the way for a more rational design of the Pt-free catalysts.

2. Results and Discussion

2.1. Material Synthesis and Characterization

$Ni/Ni(OH)_2/C$ was synthesized via liquid-phase chemical reduction method. Subsequently, $Pd_xRu_y/Ni(OH)_2/C$ with the structure of Pd, Ru co-deposition on $Ni(OH)_2$ with high dispersion via galvanic replacement method (**Figure 1**a and Experimental Section). Herein, the amount of adding Pd and Ru precursors was precisely controlled to design systems with different Pd and Ru loadings (different Pd/Ru atomic ratios). Simultaneously, the exact metal loadings were determined by inductively coupled plasma mass spectrometry (ICP-MS) (Table S1, Supporting Information). As shown in Table S1 (Supporting Information), the metal loadings in $Pd_{12}Ru_3/Ni(OH)_2/C$ with Pd (3.94 wt.%) and Ru (0.98 wt.%) are substantially lower than commercial Pt/C (20 wt.%), and Pd/C (10 wt.%). Crystallite structures of as-obtained materials were identified through powder X-ray diffraction (XRD) (Figure S1, Supporting Information). The crystal phases of the $Ni/Ni(OH)_2/C$ and $Pd_{12}Ru_3/Ni(OH)_2/C$ catalysts were determined as $Ni(OH)_2$. The signal peaks of Pd or Ru could not be observed, further confirming the very high dispersion of both elements in these materials. Spherical aberration-corrected scanning transmission electron microscope (AC-STEM) (Figure 1b–d) characterization shows the formation of atomic-level Pd and Ru (Pd clusters and Ru single atoms). More importantly, STEM-EDS elemental mapping in the region of Figure 1d presents the wide signal distribution range of Ni (Figure 1e). Pd and Ru species are found to be uniformly distributed in the material, with the intensity much lower than Ni (Figure 1f,g). Especially, the bright dots marked with the blue circles are ascribed to Ru single atoms (Figure 1b,c). Indicated red ellipses represent the Pd clusters (Figure 1b,c). The obvious lattice fringes (2.32 Å) could be assigned to $Ni(OH)_2$(111) plane (Figure 1c). These findings demonstrate that $Pd_{12}Ru_3/Ni(OH)_2/C$ possesses a unique nanostructure of Pd clusters and Ru single atoms on the $Ni(OH)_2$ nanoparticles. The relative metal content in the $Pd_{12}Ru_3/Ni(OH)_2/C$ catalyst was determined by STEM elemental line-scanning (Figure 1h,i). The content of Ni is much higher than that of Pd, and Ru possesses the lowest content (Figure 1i). X-ray photoelectron spectroscopy (XPS) was utilized to probe the chemical state and composition on the catalyst's surface as well as the binding status of as-obtained catalysts (Figures S2 and S3, Supporting Information). XPS spectra reflect that the Ni species is mainly in the form of $Ni(OH)_2$, Pd is together with Pd(0) and Pd^{n+} (the content of Pd^{n+} >> that of Pd(0) owing to surface oxidation of Pd clusters in the air). Additionally, the poor signal of Ru 3p XPS indicates the low content of Ru in $Pd_{12}Ru_3/Ni(OH)_2/C$, which further confirms the conclusion that Ru species probably exist as single atoms (Figure S2, Supporting Information). The binding

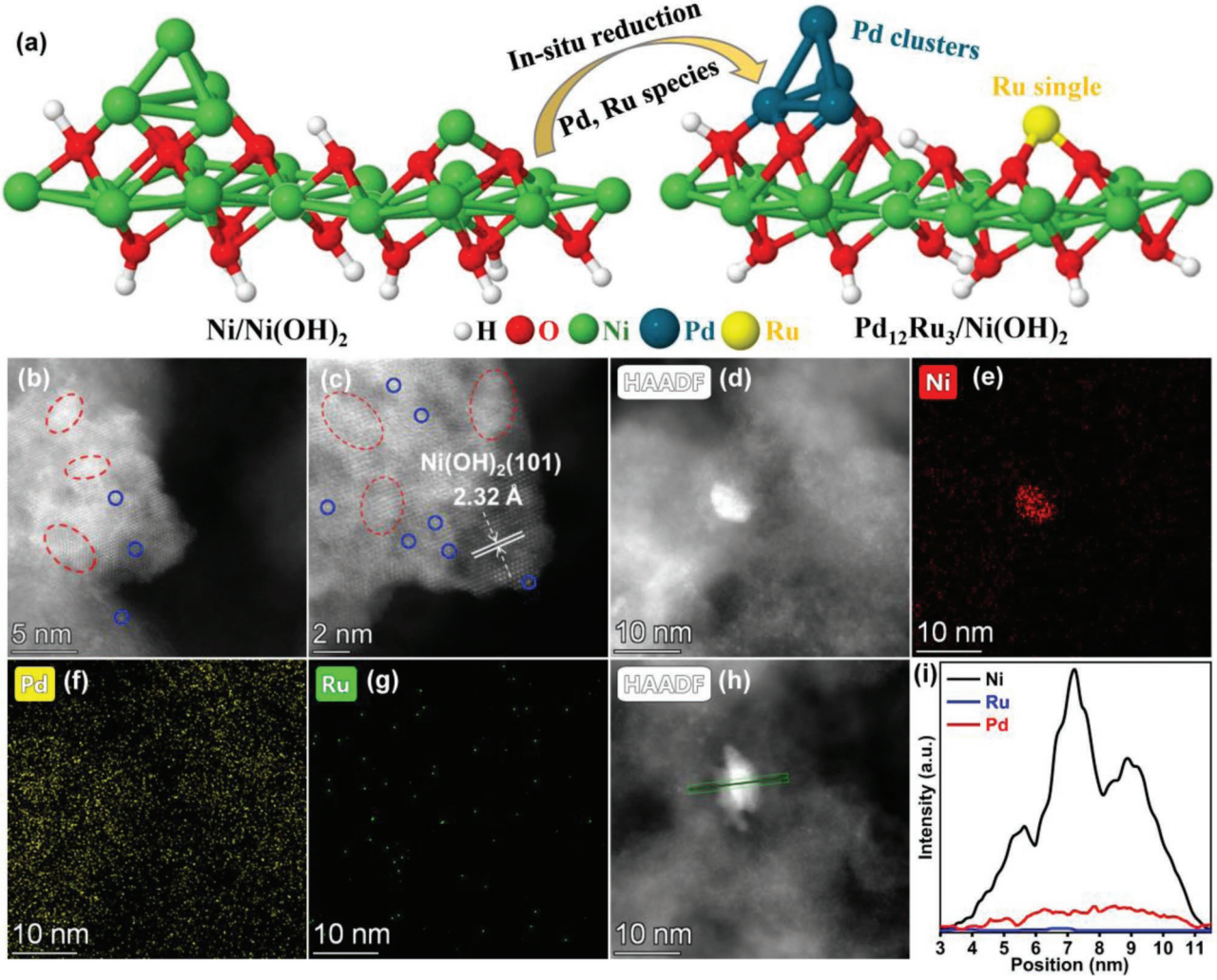

Figure 1. Synthesis and structural characterization of $Pd_{12}Ru_3/Ni(OH)_2/C$. a) Schematic illustration of preparing $Pd_xRu_y/Ni(OH)_2/C$. AC-STEM images of $Pd_{12}Ru_3/Ni(OH)_2/C$. Scale bars: b) 5, c) 2 ,and d) 10 nm. e–g) The AC-STEM-EDS elemental maps of $Pd_{12}Ru_3/Ni(OH)_2/C$, e) Ni, f) Pd, and g) Ru. h) AC-STEM image, scale bar: 10 nm, and i) corresponding elemental line-scanning profiles.

energies of Pd 3d in $Pd_{12}Ru_3Ni_{85}/C$ show a negative shift relative to $Pd_{12}Ru_3/Ni(OH)_2/C$ after thermal reduction treatment in $90\%N_2+10\%H_2$. It illustrates that the binding energy decreases significantly when the oxidation state content decreases due to the formation of PdRuNi alloy (Figure S3, Supporting Information). The surface metal contents of $Pd_{10}Ru_5/Ni(OH)_2/C$, $Pd_{12}Ru_3/Ni(OH)_2/C$, $Pd_{14}Ru_1/Ni(OH)_2/C$, and $Pd_{12}Ru_3Ni_{85}/C$ were further measured by using high sensitivity low energy ion scattering (HS-LEIS) spectra. The contents of Pd and Ru on the $Pd_{12}Ru_3/Ni(OH)_2/C$ surface reduce after thermal reduction treatment, obtaining the $Pd_{12}Ru_3Ni_{85}/C$ (Figure S4, Supporting Information).

XAS tests were performed to further investigate the local structures at the atomic level, nanostructures, and chemical state of different elements of as-obtained samples ($Pd_{12}Ru_3/Ni(OH)_2/C$, $Pd_{12}Ru_3Ni_{85}/C$), XANES, and EXAFS spectra of these catalysts and the reference compound (Ni-foil, NiO, Ni_2O_3, $Ni(OH)_2$, Ru-foil, RuO_2, $RuCl_3$, Pd-foil, and PdO) are shown in **Figure 2**. In the XANES spectra of Pd *K*-edge (Figure 2a), the energy position of near-edge absorption and the white line intensity for $Pd_{12}Ru_3Ni_{85}/C$ is very close to Pd foil, indicating that Pd is in a zero valence state. However, the Pd *K*-edge XANES spectrum of $Pd_{12}Ru_3/Ni(OH)_2/C$ is located between Pd foil and PdO, demonstrating that Pd is in the form of $Pd^{\delta+}$ species. The existing difference in the Pd valence state in these two catalysts is because PdRuNi alloy is present in $Pd_{12}Ru_3Ni_{85}/C$ and Pd clusters are coated on the surface of $Ni(OH)_2$ by the interaction of Pd-$Ni(OH)_2$ in $Pd_{12}Ru_3/Ni(OH)_2/C$. In Figure 2b, the Ru *K*-edge XANES spectrum of $Pd_{12}Ru_3Ni_{85}/C$ is almost identical to that of Ru foil, implying that the chemical state of Ru atoms is zero, but the XANES curve of $Pd_{12}Ru_3/Ni(OH)_2/C$ is close to that of RuO_2, suggesting Ru with positive charge approaching +4 (Ru single atoms easily being oxidized under air). By detailed analysis of the Ni *K*-edge XAS spectra (Figure 2c), Ni^{2+} species are dominant in $Pd_{12}Ru_3/Ni(OH)_2/C$ while Ni(0) and Ni^{2+} species are present in $Pd_{12}Ru_3Ni_{85}/C$. Furthermore, Figure 2d–f displays the EXAFS spectra of these two samples and the reference compound. In Figure 2d, there is a small amount of

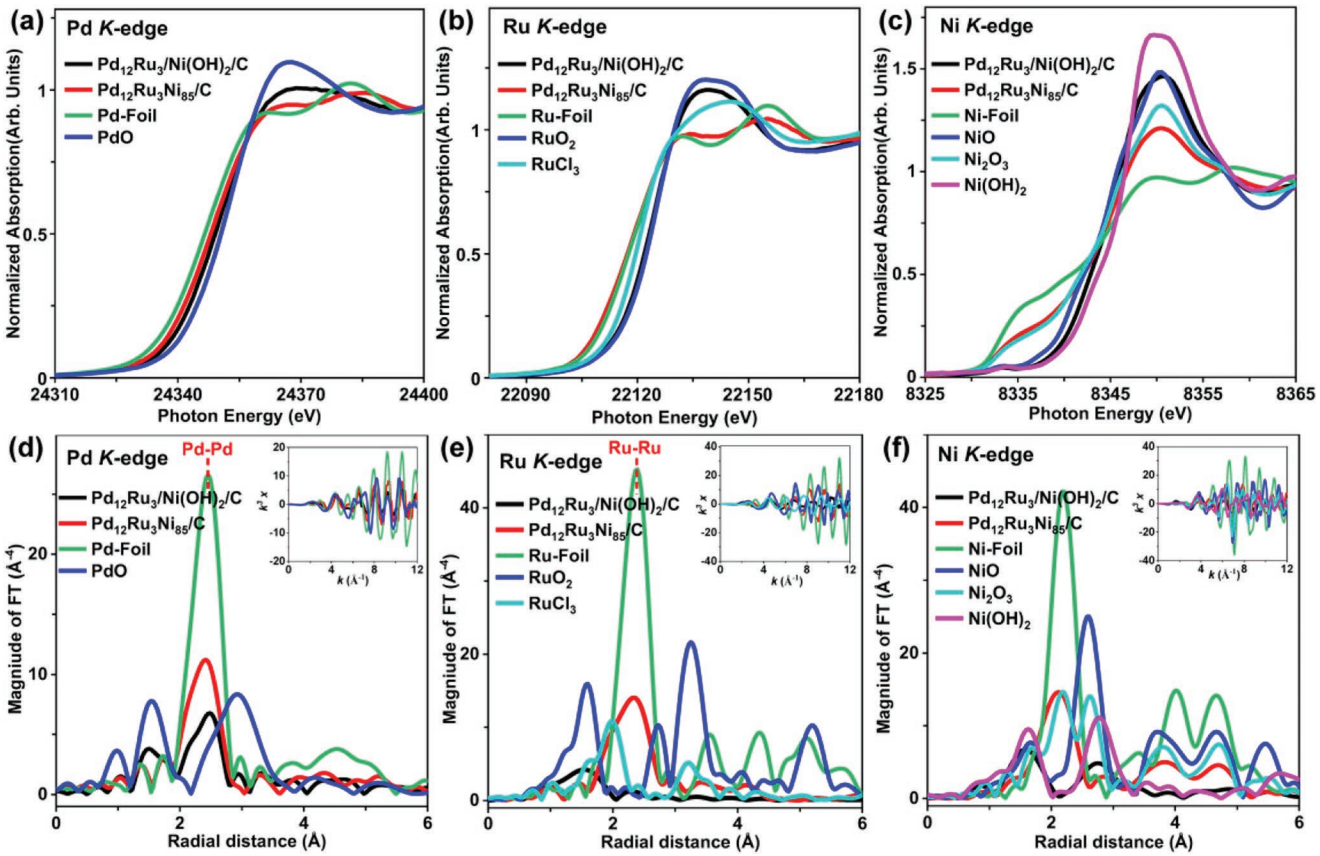

Figure 2. X-ray absorption spectra of the catalysts. XANES spectra for $Pd_{12}Ru_3/Ni(OH)_2/C$, $Pd_{12}Ru_3Ni_{85}/C$ catalysts recorded at a) Pd *K*-edge, b) Ru *K*-edge, c) Ni *K*-edge, and Fourier transformed EXAFS spectra toward d) Pd *K*-edge, e) Ru *K*-edge, f) Ni *K*-edge for the catalysts. The spectra of the reference compound Ni-foil, NiO, Ni_2O_3, $Ni(OH)_2$, Ru-foil, RuO_2, $RuCl_3$, Pd-foil, and PdO are also shown for comparison.

Pd—O bond (distance of ≈1.6 Å), with Pd—Pd bond (2.5 Å) being dominant for $Pd_{12}Ru_3/Ni(OH)_2/C$ and Pd—Pd bond (or Pd-Ni) with ≈2.4 Å distance mainly present for $Pd_{12}Ru_3Ni_{85}/C$. Moreover, the intensity of the Pd—Pd bond (or Pd—Ni) in $Pd_{12}Ru_3Ni_{85}/C$ is larger than that in $Pd_{12}Ru_3/Ni(OH)_2/C$, indicating that the content of Pd(0) significantly increases owing to the PdRuNi alloy after $Pd_{12}Ru_3/Ni(OH)_2/C$ being reduced in $90\%N_2+10\%H_2$ at 400 °C (obtaining $Pd_{12}Ru_3Ni_{85}/C$). There is only a single peak at 1.6 Å, which can be attributed to the contribution of the Pd—O bond (first shell), no peak of the Ru—Ru bond can be found (Figure 2e). This is the direct evidence that Ru is highly dispersed with single atoms coordinated by O atoms from $Ni(OH)_2$. Figure 2f reveals that the contribution of the scattering path of Ni—Ni and Ni—O is observed. In a word, all the above results illustrate that single Ru atoms and tiny Pd clusters are successfully loaded on the surface of $Ni(OH)_2$ in $Pd_{12}Ru_3/Ni(OH)_2/C$, but PdRuNi alloy forms in $Pd_{12}Ru_3Ni_{85}/C$.

2.2. Electrochemical Performance Analysis

2.2.1. Electrocatalytic Performance toward the HER

HER electrocatalytic activity of $Pd_{12}Ru_3/Ni(OH)_2/C$ in 1 M KOH electrolyte was evaluated by linear sweep voltammetry (LSV) at a scan rate of 5 mV s^{-1} (Experimental Section). All potential values in this work were calibrated to the reversible hydrogen electrode (RHE) with *iR* compensation. HER performance of $Pd_{12}Ru_3/Ni(OH)_2/C$ was remarkably superior to those of $Pd_{10}Ru_5/Ni(OH)_2/C$, $Pd_{14}Ru_1/Ni(OH)_2/C$, $Pd_{12}Ru_3Ni_{85}/C$, $Pd_{15}/Ni(OH)_2/C$, $Ru_{15}/Ni(OH)_2/C$, $Ni/Ni(OH)_2/C$, and $Pd_{12}Ru_{88}/C$. The typical polarization curve of $Pd_{12}Ru_3/Ni(OH)_2/C$ displays ultralow overpotentials of 16.1 and 97 mV to acquire the current density of 10 and 100 mA cm^{-2}, respectively, much lower than commercial Pt/C (**Figure 3**a,b,g; Figure S5, Supporting Information). HER polarization curves without *iR* correction are also presented and indicated the outstanding HER efficiency of $Pd_{12}Ru_3/Ni(OH)_2/C$ (Figure S6, Supporting Information). It is noteworthy that $Pd_xRu_y/Ni(OH)_2/C$ exhibits enhanced HER activity when compared with other reported electrocatalysts (Table S2, Supporting Information). The Tafel slope of $Pd_{12}Ru_3/Ni(OH)_2/C$, $Pd_{10}Ru_5/Ni(OH)_2/C$, and $Pd_{14}Ru_1/Ni(OH)_2/C$ was calculated to be 21.8 mV, 22.5 mV, and 26.6 mV dec^{-1}, respectively, it revealed that the conversion of adsorbed hydrogen to molecular hydrogen was a rate-determining step (Tafel slope < 30 mV dec^{-1})[38] (Figures 3c,5a). Thus, HER mechanism on $Pd_{12}Ru_3/Ni(OH)_2/C$, $Pd_{10}Ru_5/Ni(OH)_2/C$, and $Pd_{14}Ru_1/Ni(OH)_2/C$ catalyst surface is Volmer–Tafel.[39] Noteworthily, $Pd_{12}Ru_3/Ni(OH)_2/C$ is observed to possess a larger electrochemical active area than state-of-the-art commercial Pt/C and other as-prepared electrocatalysts through

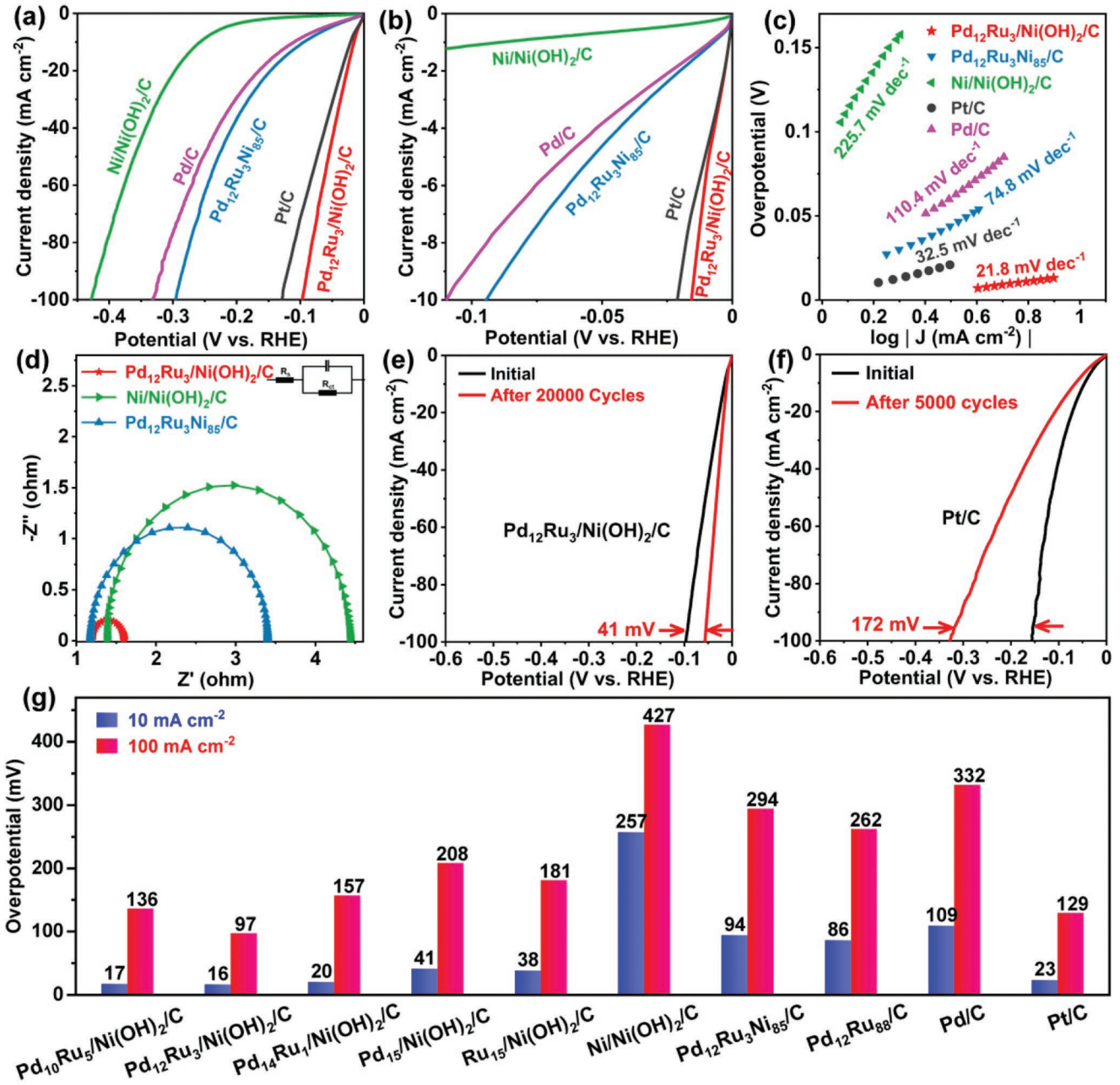

Figure 3. Electrocatalytic performance of as-obtained catalysts toward HER. a) HER polarization curves with *iR* compensation in an N_2-saturated 1.0 M KOH solution. Scan rate 5 mV s^{-1}. b) Enlarged view of (a). c) Tafel plots. d) Nyquist plots of $Pd_{12}Ru_3/Ni(OH)_2/C$, $Pd_{12}Ru_3Ni_{85}/C$, and $Ni/Ni(OH)_2/C$ in 1.0 M KOH solution. e) Polarization curves of initial $Pd_{12}Ru_3/Ni(OH)_2/C$, after 20 000 cycles. f) Polarization curves of initial Pt/C after 5000 cycles. g) Overpotential of as-obtained catalysts at 10 and 100 mA cm^{-2}.

recording CV curves from 0.2 to 0.4 V (non-faraday region) at scan rates of 10–50 mV s^{-1} (Figure S7, Supporting Information). It suggests that the synergistic interaction of Ru single atom, Pd clusters, and $Ni(OH)_2$ nanoparticles as well as the existence of multiple-metal synergistic effect is conducive to an optimum electrochemically active area.

Electrochemical impedance spectroscopy measurements were also conducted to further reveal the HER kinetics of as-obtained catalysts. The Nyquist plots and enlarged Nyquist plots in the high-frequency region are estimated and exhibited for comparison (Figure 3d; Figures S8d and S9, Supporting Information). $Pd_{12}Ru_3/Ni(OH)_2/C$ with $Ni(OH)_2$ exhibited smaller charge transfer resistance (R_{ct}), indicating that the $Pd_{12}Ru_3/Ni(OH)_2/C$ catalyst had higher intrinsic activity than $Pd_{12}Ru_3Ni_{85}/C$ and $Ni/Ni(OH)_2/C$ for alkaline HER. The higher intrinsic activity was derived from the synergistic effect among $Ni(OH)_2$ edge sites, Ru single atoms, and Pd clusters, expediting the water decomposition step (Step 1, Volmer step) and hydrogen formation step (Step 2, Tafel step). Stability is a crucial issue for the development of single atomic electrocatalysts.

Hence, the cyclic stability of $Pd_{12}Ru_3/Ni(OH)_2/C$ was evaluated by comparing the LSV curves before and after 20 000 cycles from 0 to –0.6 V (vs RHE) with 50 mV s^{-1} in 1 M KOH solution. $Pd_{12}Ru_3/Ni(OH)_2/C$ even exhibited enhanced HER performance and the polarization potential of $Pd_{12}Ru_3/Ni(OH)_2/C$ decreased by 41 and 50 mV after long-term stability for 20 000 cycles at 100 and 360 mA cm^{-2} (Figure 3e;Figure S10a, Supporting Information). In contrast, commercial Pt/C could not achieve a large current density of 360 mA cm^{-2} but only 230 mA cm^{-2}, suggesting its inferior catalytic activity for the HER. In addition, commercial Pt/C demonstrated a 390 mV enhancement of the polarization potential at 230 mA cm^{-2} after long-term stability for only 5000 cycles (Figure 3f; Figure S10b, Supporting Information). Unexpectedly, after 20 000 cycles of HER, the crystal structure and size of the $Ni(OH)_2$ nanoparticles were still almost maintained, indicating that the strong interaction of Ru single atoms, Pd nanoclusters, and $Ni(OH)_2$ enhanced HER stability (Figures S11 and S12, Supporting Information). XPS results suggest that the surface metal content of $Pd_{12}Ru_3/Ni(OH)_2/C$ increases due to the electrochemical activation of surface metal sites after long-time HER measurements (Figure S13, Supporting Information).

2.2.2. Electrocatalytic Performance toward the EOR

All samples were controlled to have identical loading (10 µL, 2 mg mL^{-1}) on the working electrode (Experimental Section). EOR electrochemical measurements were performed with a three-electrode cell in 1 M KOH + 1 M C_2H_5OH electrolyte. The correlative CV curves were recorded till EOR performance was stable. Two characteristic oxidation peaks of the EOR appear toward the Pd-based catalysts in 1 M KOH + 1 M C_2H_5OH solution. The peak current of the forward scan is widely considered to be due to ethanol oxidation while the other peak current in the backward scan is ascribed to further oxidation of intermediates (e.g., CH_3COO_{ad} and CO_{ad}) generated from the forward scan.[40] It clearly shows that $Pd_{12}Ru_3/Ni(OH)_2/C$ possesses significantly enhanced mass activity (much higher than $Pd_{10}Ru_5/Ni(OH)_2/C$ and $Pd_{14}Ru_1/Ni(OH)_2/C$) (**Figure 4**a,b), suggesting that regulation toward EOR reactivity can be finely tuned by controlling the atomic ratio of Pd/Ru. The mass activity of $Pd_{12}Ru_3/Ni(OH)_2/C$ was 3.724 A mg_{PdRu}^{-1} (5.93 times over $Pd_{12}Ru_3Ni_{85}/C$ and 19.5 times over Pd/C, respectively) (Figure 4f; Table S3, Supporting Information) and showed enhanced mass activity during the comparison of the EOR activity between $Pd_xRu_y/Ni(OH)_2/C$ and previously reported electrocatalysts (Table S4, Supporting Information). The electrocatalytic performance of $Pd_{12}Ru_3Ni_{85}/C$ was inferior to $Pd_{12}Ru_3/Ni(OH)_2/C$, indicating the importance of the metal hydroxide support for the electrocatalytic ethanol oxidation reaction (Figure 4b; Table S3, Supporting Information). CO-stripping experiments of $Pd_{12}Ru_3/Ni(OH)_2/C$, $Pd_{15}/Ni(OH)_2/C$, $Pd_{12}Ru_3Ni_{85}/C$, and Pd/C were carried out to evaluate CO tolerance. $Pd_{12}Ru_3Ni_{85}/C$ shows negative onset potential (0.65 V vs RHE) to Pd/C (0.72 V), demonstrating that the tri-component synergy (Pd, Ru, and $Ni(OH)_2$) could facilitate CO oxidation. $Pd_{12}Ru_3/Ni(OH)_2/C$ exhibited a negative onset potential (0.23 V vs RHE) to $Pd_{12}Ru_3Ni_{85}/C$ (0.65 V vs RHE) and $Pd_{15}/Ni(OH)_2/C$ (0.41 V vs RHE), confirming that the existence of $Ni(OH)_2$ and the doping of Ru single atoms and Pd clusters results in the promotion of CO oxidation (Figure 4c). The electrochemically active specific area of $Pd_{12}Ru_3/Ni(OH)_2/C$ (84.6 m^2 g_{Pd}^{-1}) determined by CO-stripping experiments was superior to that of $Pd_{15}/Ni(OH)_2/C$ catalyst (72.4 m^2 g_{Pd}^{-1}), $Pd_{12}Ru_3Ni_{85}/C$ (48.3 m^2 g_{Pd}^{-1}),and commercial Pd/C (28.6 m^2 g_{Pd}^{-1}). More importantly, the specific activity (ECSA normalized) of $Pd_{12}Ru_3/Ni(OH)_2/C$ was 1.75 times over $Pd_{12}Ru_3Ni_{85}/C$ and 2.96 times over commercial Pd/C (Figure 4d). Additionally, $Pd_{12}Ru_3/Ni(OH)_2/C$ also exhibited outstanding stability during the long-term chronoamperometry durability measurement at 0.757 V (vs RHE) in 1 M C_2H_5OH + 1 M KOH in comparison with other catalysts (Figure 4e).

To investigate the relevance between the excellent durability and the crystallite structure, size of $Pd_{12}Ru_3/Ni(OH)_2$, XRD, TEM, and HRTEM characterization of $Pd_{12}Ru_3/Ni(OH)_2/C$ after chronoamperometry were also performed. No significant changes in crystalline structure and dispersion of the $Ni(OH)_2$ nanoparticles (still highly uniform without obvious agglomeration) could be observed, proving the remarkable stability of $Pd_{12}Ru_3/Ni(OH)_2$ in the EOR (Figures S14, and S15, Supporting Information). XPS spectra of $Pd_{12}Ru_3/Ni(OH)_2$ after chronoamperometry also show unchanged binding energies for Pd 3d, Ru 3p, and Ni 2p as compared to those of the fresh $Pd_{12}Ru_3/Ni(OH)_2$, indicating that the synergistic effect among Pd, Ru, and $Ni(OH)_2$ enhances chronoamperometry stability. The intensity of Pd 3d, Ru 3p, and Ni 2p increases due to the electrochemical activation of the $Pd_{12}Ru_3/Ni(OH)_2$ catalyst surface during the chronoamperometry stability test (Figure S16, Supporting Information).

2.3. Electrocatalytic Mechanism on $Pd_{12}Ru_3/Ni(OH)_2/C$

2.3.1. Operando Raman Spectra Measurements in the HER

Operando Raman spectra were further obtained to uncover the dynamic surface chemistry of $Pd_{12}Ru_3/Ni(OH)_2$ during the HER. The vibration peaks of Ni—OH and Ni—O are observed in the range of 400–600 cm^{-1} of ex situ Raman (**Figure 5**a),[41,42] and disappeared after $Pd_{12}Ru_3/Ni(OH)_2/C$ is immersed in 1 M KOH solution of open circuit spectra (OCP), which should be ascribed to the scattering of Raman signal by the electrolyte. Interestingly, the growing intensity of Ni—OH and Ni—O vibration toward $Pd_{12}Ru_3/Ni(OH)_2/C$ with increasing applied potential is obvious, indicating the formation of $Ni—OH_{ad}$ (Figure 5a). When the potential decreases back to OCP, these Raman bands are weakened and similar to ex situ Raman that is different from initial OCP, confirming water decomposition on Ni^{2+} defect sites (Figure 5b). Apparently, after the introduction of nickel (hydr)oxides, $Pd_{12}Ru_3/Ni(OH)_2/C$ shows a faster water dissociation kinetics because oxygen atoms could be easily adsorbed and activated at positively charged Ni sites to form the $Ni—OH_{ad}$. Meanwhile, H* is transferred to the Pd nanoclusters and Ru single atoms to form Pd—H* or Ru—H*. Therefore, the synergetic effect is significant for promoting the HER rate-determining step (Volmer step). By contrast, $Ni—OH_{ad}$ signals are also capable of discovering on $Pd_{12}Ru_3Ni_{85}/C$ but requiring

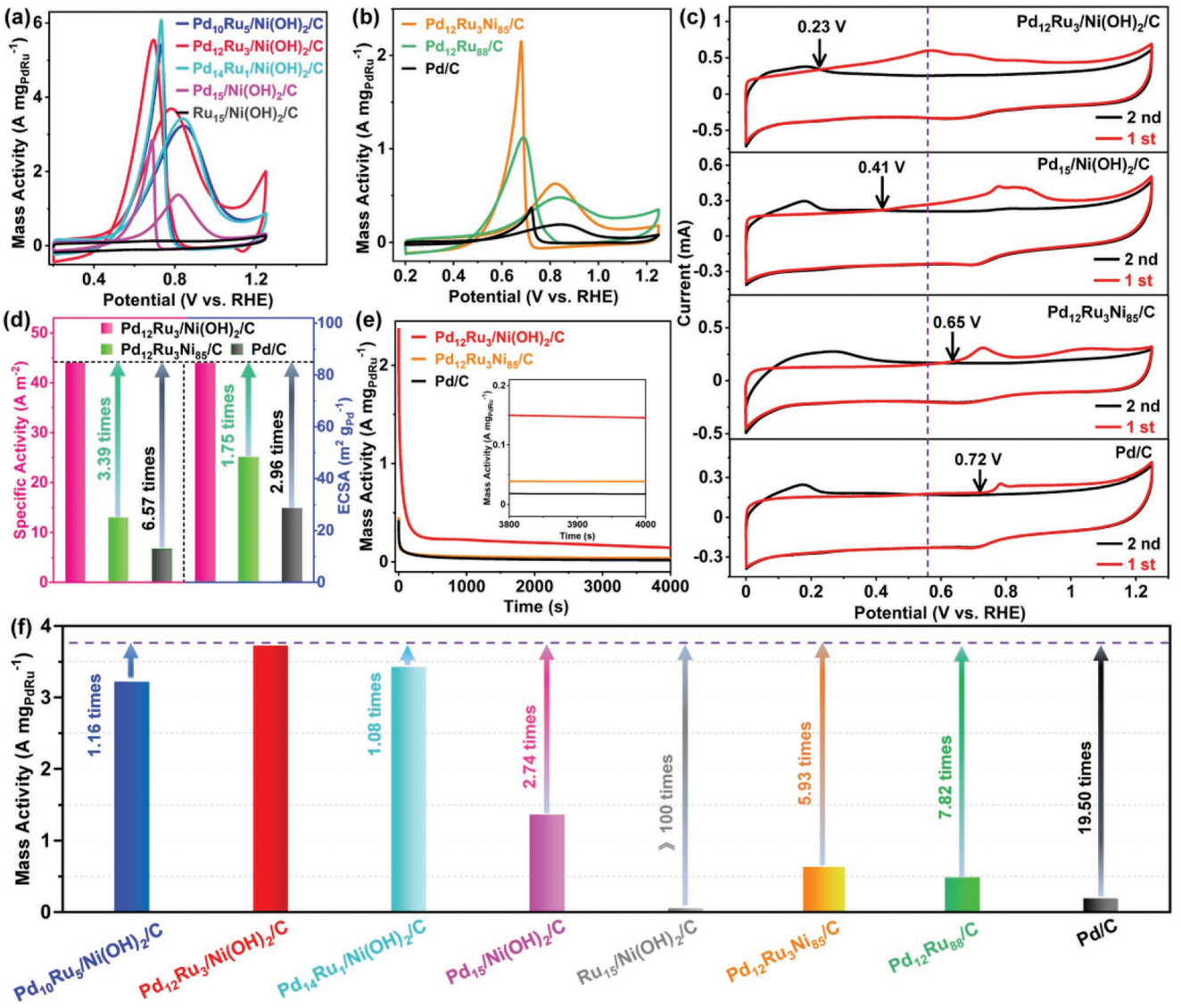

Figure 4. Electrocatalytic performance toward the EOR. a,b) Electrocatalytic performance of as-prepared catalysts toward the EOR: PdRu loading-normalized of cyclic voltammograms for the EOR recorded in 1 M KOH + 1 M C_2H_5OH solution. Scan rate, 50 mV s^{-1}. c) CO-stripping experiments of $Pd_{12}Ru_3/Ni(OH)_2/C$, $Pd_{15}/Ni(OH)_2/C$, $Pd_{12}Ru_3Ni_{85}/C$, and commercial 10 wt.% Pd/C, d) The specific activity (ECSA normalized) toward $Pd_{12}Ru_3/Ni(OH)_2/C$, $Pd_{12}Ru_3Ni_{85}/C$, commercial 10 wt.% Pd/C, and their ECSA comparison. e) Chronoamperometry of $Pd_{12}Ru_3/Ni(OH)_2/C$, $Pd_{12}Ru_3Ni_{85}/C$, and Pd/C at 0.757 V (vs RHE) for 4000 s. f) the mass activity of as-obtained catalysts.

higher applied potential, suggesting a positive contribution of nickel (hydr)oxides to H_2O adsorption and dissociation processes (Figure 5c,d). HER mechanism of $Pd_{12}Ru_3/Ni(OH)_2/C$ for hydrogen evolution in 1 M KOH is displayed in Figure 5e. The synergistic effect among $Ni(OH)_2$ edge sites, Ru single atoms, and Pd clusters expedites the water decomposition step (Step 1, Volmer step) and hydrogen formation step (Step 2, Tafel step).

2.3.2. In Situ FTIR Measurements in EOR

The EOR process is considered to be a dual-path reaction pathway of C_1 and C_2 pathways simultaneously, which is an extremely complicated process.[43,44] It is well known that the C_2 pathway with four electrons transfer is more likely to occur for the EOR, generating CH_3COOH and CH_3CHO_{ad} intermediates.[43,44] However, CH_3COOH is extremely difficult to be further oxidized to CO_2, resulting in the EOR efficiency deterioration. Compared with C_2, the C_1 pathway generates a higher energy density with 12 electrons delivered and the C_2H_5OH molecule is oxidized to produce CO_2.[45,46] It is expected to improve the ratio of the C_1 pathway by the catalyst design for efficient utilization of ethanol. To understand the role of Ru single atom and $Ni(OH)_2$ in the EOR, in situ Fourier transform infrared (FTIR) reflection spectroscopy measurements were used to qualitatively analyze reaction species and quantitative calculated CO_2 selectivity. By calculating with reference

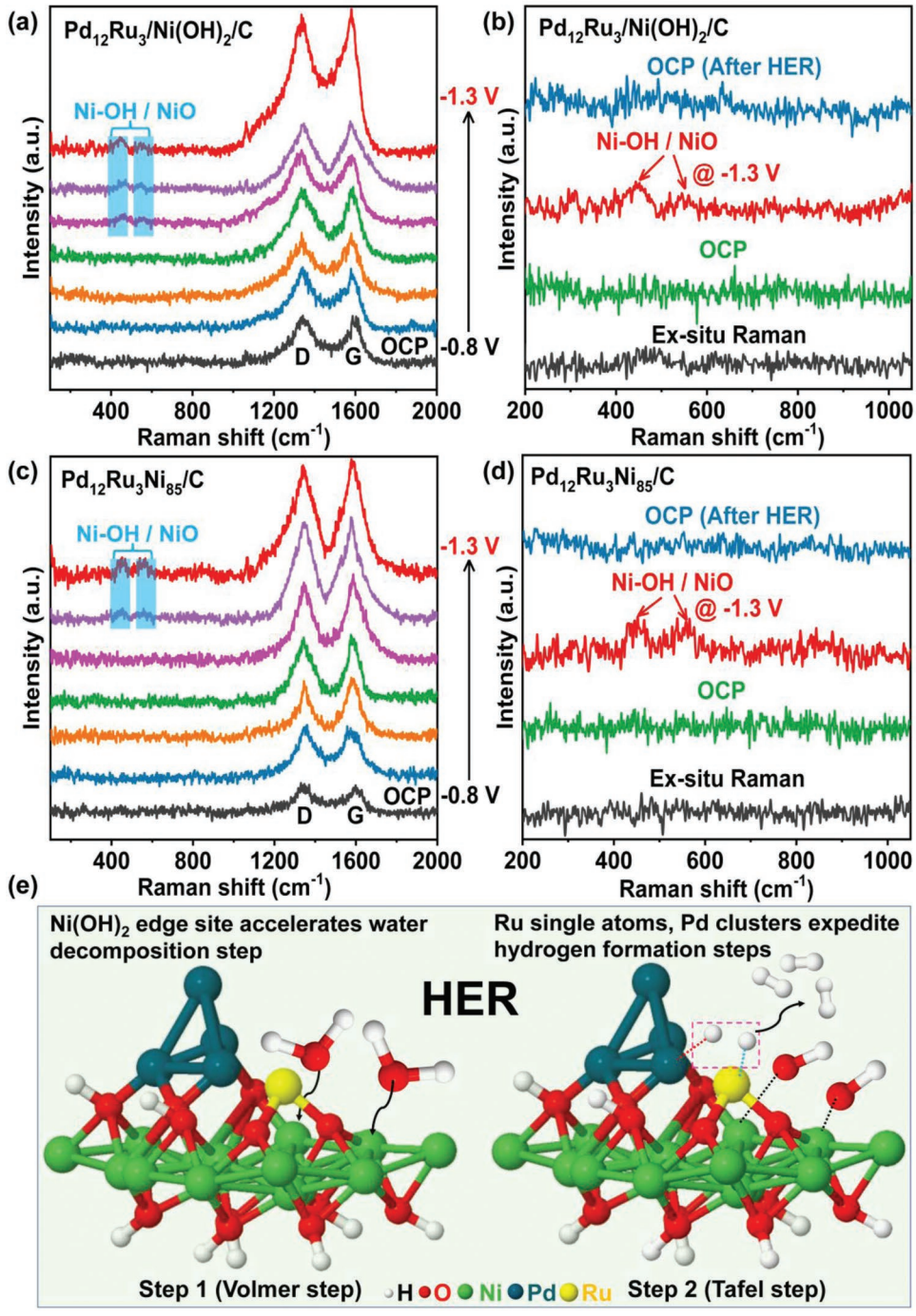

Figure 5. HER synergistic mechanism and Operando Raman spectra. a) Operando Raman spectra at OCP and different applied potentials (vs Hg/HgO) in 1 M KOH for $Pd_{12}Ru_3/Ni(OH)_2/C$ and b) Ex situ Raman, OCP, and Operando Raman spectra of $Pd_{12}Ru_3/Ni(OH)_2/C$ at –1.3 V (vs Hg/HgO), and OCP after the HER, c) $Pd_{12}Ru_3Ni_{85}/C$ and d) ex situ Raman, OCP, and Operando Raman spectra of $Pd_{12}Ru_3Ni_{85}/C$ at –1.3 V (vs Hg/HgO), and OCP after HER, e) The synergistic effect among $Ni(OH)_2$ edge sites, Ru single atoms, and Pd clusters expedites the water decomposition step (Step 1, Volmer step) and hydrogen formation step (Step 2, Tafel step).

potential (E_r) at 0.1 V, the research potential (E_s) spectrum is collected from 0.2 to 1.4 V at 0.1 V intervals and the spectra of $Pd_{12}Ru_3/Ni(OH)_2/C$, $Pd_{12}Ru_3Ni_{85}/C$, and commercial Pd/C is showed in **Figure 6**a,d,g. Owing to utilizing the relative change method, the upward and downward bands in the spectra represent consumed and generated species, respectively. The upward bands of 1084 and 1048 cm^{-1} could be assigned to the C—O stretching vibration of ethanol (while the increasing band intensity is corresponding to ethanol being oxidized). The downward bands at 1550 and 1414 cm^{-1} can be assigned to the asymmetric

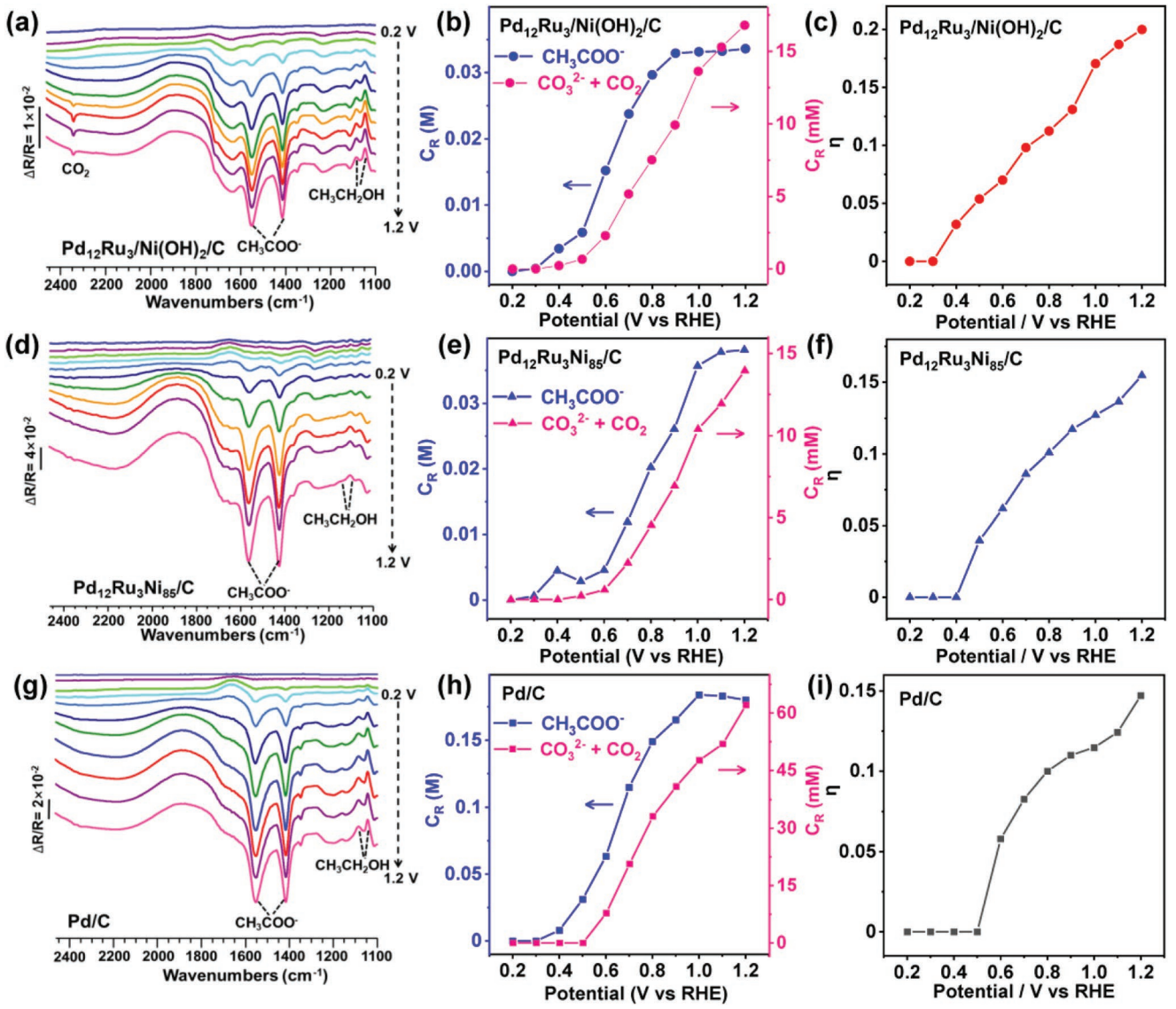

Figure 6. Electrochemical in situ FTIR for the EOR. a) $Pd_{12}Ru_3/Ni(OH)_2/C$, d) $Pd_{12}Ru_3Ni_{85}/C$, and g) commercial Pd/C in 1 M KOH + 1 M CH_3CH_2OH solution at 0.2 to 1.2 V (vs RHE). Potential dependence of relative concentration (CR) of CH_3COO^-, CO_3^{2-}, and CO_2 generated from ethanol oxidation on b) $Pd_{12}Ru_3/Ni(OH)_2/C$, e) $Pd_{12}Ru_3Ni_{85}/C$, and h) Pd/C. Potential dependence of the selectivity for complete ethanol oxidation to CO_2 and CO_3^{2-}: c) $Pd_{12}Ru_3/Ni(OH)_2/C$, f) $Pd_{12}Ru_3Ni_{85}/C$, and i) Pd/C.

and symmetric stretching vibrations of O—C—O in CH_3COO^- ions. However, overlapping the peak of carbonate ions (CO_3^{2-}) at 1390 cm^{-1}, the latter band at 1414 cm^{-1} has higher intensity. Compared to $Pd_{12}Ru_3Ni_{85}/C$ and commercial Pd/C, a new generated band at 2345 cm^{-1} appears at 0.8 V and band intensity increases with the potentials for $Pd_{12}Ru_3/Ni(OH)_2/C$. The downward at 2345 cm^{-1} can be defined as an asymmetric vibration band of CO_2, indicating that $Pd_{12}Ru_3/Ni(OH)_2/C$ could generate more CO_2 by the C_1 pathway. To clarify the C—C cleavage ability of different nanocatalysts, the concentration of the reaction products in the EOR was quantitatively analyzed by subtracting with standard spectra reported in previous work.[47] The illustration of the subtracting procedure of IR spectra is displayed in Figure S17 (Supporting Information). The concentrations of C_2 product (CH_3COO^-) and C_1 products (CO_3^{2-} and CO_2) of $Pd_{12}Ru_3/Ni(OH)_2/C$, $Pd_{12}Ru_3Ni_{85}/C$, and commercial Pd/C are shown in Figure 6b,e,h, and carbon dioxide selectivity (η) are further calculated by the following formula:

$$\eta = \frac{\left(C\left[CO_3^{2-}\right] + C\left[CO_2\right]\right)/2}{C\left[CH_3COO^-\right] + \left(C\left[CO_3^{2-}\right] + C\left[CO_2\right]\right)/2} \quad (1)$$

Compared to the generated potential of C_1 products, $Pd_{12}Ru_3/Ni(OH)_2/C$ produces carbonate ions at 0.4 V and is lower than $Pd_{12}Ru_3/Ni(OH)_2/C$ at 0.5 V and commercial Pd/C at 0.6 V. $Ni(OH)_2$ could probably produce OH_{ad} species at the low potential to oxidize CO and CH_x to CO_2, consistent with CO oxidation measurements.[48,49] Moreover, as shown in Figure 6c,f,i $Pd_{12}Ru_3/Ni(OH)_2/C$ exhibited a remarkable CO_2

selectivity (20.9%) as compared to $Pd_{12}Ru_3Ni_{85}/C$ (15.5%) and commercial Pd/C (14.7%), which might be attributed to nearby Ru and $Ni(OH)_2$ producing OH_{ad} species at the lower potential, improving the ability of further oxidation removal of intermediate products.[50] The EOR mechanism of $Pd_{12}Ru_3/Ni(OH)_2/C$ is displayed in Figure S18 (Supporting Information). The synergistic effect among $Ni(OH)_2$ edge site, Ru single atoms, and Pd clusters: $Ni(OH)_2$ edge site, Ru single atoms provide adsorbed OH*, Pd clusters adsorb ethanol, and the adjacent OH* expedites elimination of the CO_{ad} to avoid Pd being poisoned (Figure S18, Supporting Information).

3. Conclusion

$Pd_xRu_y/Ni(OH)_2/C$ catalysts were rationally designed with various Pd/Ru atomic ratios by a simple approach for the deposition of Ru single atoms and Pd clusters on $Ni(OH)_2$. As-synthesized $Pd_{12}Ru_3/Ni(OH)_2/C$ displayed superior performance both in the HER and EOR processes as compared to commercial Pt/C and Pd/C. The overpotential of $Pd_{12}Ru_3/Ni(OH)_2/C$ for HER significantly decreased to 16.1 mV@10 mA cm^{-2} with the Tafel slope of 21.8 mV dec^{-1} and was superior to commercial Pt/C (26.0 mV@10 mA cm^{-2} and 32.5 mV dec^{-1}, respectively). $Pd_{12}Ru_3/Ni(OH)_2/C$ even displayed enhanced HER efficiency even after 20 000 cycles of stability test. Noteworthy, the existence of Pd nanoclusters, Ru single atoms not only have effectively boosted the rate-determining step (Tafel step) of adsorbed hydrogen converting to molecular hydrogen but also improved the intrinsic activity of $Ni(OH)_2$ for high-efficiency water decomposition. Besides, the mass activity of $Pd_{12}Ru_3/Ni(OH)_2/C$ for EOR was 3.724 A mg_{PtPd}^{-1} (19.5 times higher than Pd/C). The optimized CO_2 selectivity (20.9%) of $Pd_{12}Ru_3/Ni(OH)_2/C$ could be ascribed to the synergistic and electronic effect of adjacent Ru and Pd, and the OH_{ad} adsorption by $Ni(OH)_2$ at low potential, resulting in reducing the reaction barrier for eliminating the reactant intermediate (CO_{ad}, $CH_3COO_{ad,}$ etc.) and improving the selectivity of CO_2 pathway rather than CH_3COO^- pathway. This work provides an original and novel strategy for the development of high-performance Pt-free bi-functional electrocatalysts for fuel cells and the electrolysis of water.

4. Experimental Section

Synthesis of $Pd_{12}Ru_{88}/C$: First, carbon black (BP-2000, 0.100 g) was suspended in ultrapure water (50 mL) with ultrasonic 0.5 h. Then, the palladium (II)-ammonium chloride ($(NH_4)_2PdCl_4{\cdot}H_2O$) solution and the ruthenium chloride ($RuCl_3$) solution were mixed and stirred for 1 h. After that, the solvent was steamed with a water bath (80 °C) to obtain the hybrid and reduced at 400 °C in 90%N_2 + 10%H_2 for 2 h to get the $Pd_{12}Ru_{88}/C$ sample.

Synthesis of $Ni/Ni(OH)_2/C$: A corresponding amount of nickel chloride hexahydrate ($NiCl_2{\cdot}6H_2O$) solution was mixed in ultrapure water (100 mL) and vigorously stirred for 0.5 h. Then, NaOH (1.831 g) was dissolved in ultrapure water (10 mL) and injected into the mixture dropwise. After that, hydrazine hydrate (85 wt.%, 25 mL) was added to the mixture, and carbon black was added (1.250 g). The reduction of Ni^{2+} gradually proceeded with mechanical stirring for 18.5 h. After filtration and vacuum drying at 60 °C, $Ni/Ni(OH)_2/C$ was obtained.

Synthesis of $Pd_xRu_y/Ni(OH)_2/C$: The $Ni/Ni(OH)_2/C$ catalyst (0.100 g) was suspended in ultrapure water (200 mL). The mixture was cooled by a sustained ice bath, and the aqueous $(NH_4)_2PdCl_4{\cdot}H_2O$ solution was added drop by drop. After magnetically stirring for 2 h, the $RuCl_3$ aqueous solution was appended to the mixture. After 2 h, the operation of filtration and desiccation were performed to gain the $Pd_{12}Ru_3/Ni(OH)_2/C$ catalysts. The $Pd_{10}Ru_5/Ni(OH)_2/C$ and $Pd_{14}Ru_1/Ni(OH)_2/C$ catalysts were prepared by regulating the volume of the noble metal precursor of $(NH_4)_2PdCl_4{\cdot}H_2O$ and $RuCl_3$. Moreover, the $Pd_{15}/Ni(OH)_2/C$ and $Ru_{15}/Ni(OH)_2/C$ were synthesized by the same method by adding the Pd and Ru precursors, respectively.

Synthesis of $Pd_{12}Ru_3Ni_{85}/C$: The $Pd_{12}Ru_3Ni_{85}/C$ catalyst was gained through a certain amount of $Pd_{12}Ru_3/Ni(OH)_2/C$ being reduced at 400 °C in 90%N_2 + 10%H_2 for 2 h.

Materials Characterization: The XRD by using an X-ray diffractometer (Ultima IV, Rigaku, Japan) equipped with the radiation of Cu *Ka* (40 kV, 30 mA) measurements were performed at an angle range of 10°–90°. The actual metal contents of as-obtained catalysts were measured by the inductively coupled plasma mass spectrometry (Agilent 7700 ICP-MS) technique. The electronic structures and chemical states were investigated through X-ray photoelectron spectroscopy by scanning ESCA micro-probe matching PHI Quantum 2000 with Al *Ka* (1486.6 eV) homochromous radiation. Binding energies were corrected by employing the adventitious C 1s peak at 284.6 eV as a reference. The surface metal content was determined by high sensitivity-low energy ion scattering spectroscopy (HS-LEIS, IonTOF Qtac100) equipping with the ion beam of 3 keV He^+ and 5 keV 20 Ne^+ as the sputtering ion source. The images of the catalysts were obtained by the TEM and HRTEM (TECNAI F30, 300 kV, FEI). The aberration-corrected scanning transmission electron microscope (AC-STEM, Titan Themis 60–300, FEI) combined with a Cs-corrector was employed to acquire the AC-STEM images, AC-STEM elemental maps, and line-scanning profiles of the samples at 200 kV.

X-Ray Absorption Spectra Measurements: The X-ray absorption spectra data (including XANES and EXAFS) of Ni *K*-edge, Ru *K*-edge, and Pd *K*-edge for as-synthesized samples and Ni-foil, NiO, Ni_2O_3, $Ni(OH)_2$, Ru-foil, RuO_2, $RuCl_3$, Pd-foil, and PdO were collected at beamline TPS BL44A at National Synchrotron Radiation Research Center (NSRRC), Taiwan. All data were collected at ambient temperature in transmission mode. Other experimental steps and details were similar to the previous work.[51,52] And data proceeding method was identical to the reported reference.[53]

Electrochemical Operando Raman Spectra Measurements: The measurements of Operando Raman were carried out through the Horiba HR-800 Raman microspectrometer. The working electrode (carbon paper, 1 × 1 cm^2) covered catalyst was obtained in the same way as the HER, and the reference electrodes (Hg/HgO) and the counter electrodes (graphite rod) were applied. The proton exchange membrane used for the separator experiments in a two-compartment electrochemical cell was Nafion 117 (Sigma–Aldrich). Raman spectra at –0.8–1.3 V were recorded by a CHI 650 electrochemical workstation by combining with a typical electrochemical Raman spectroscopy setup.

Electrochemical In Situ FTIR Spectra Measurements: The measurement of electrochemical in situ Fourier transform infrared (in situ FTIR) reflection spectroscopy was conducted on a Nicolet-8700 spectrometer containing a liquid-nitrogen-cooled MCT-A detector. The species (absorbed and dissolved) were measured on a thin layer (<10 mm) toward the working electrode and CaF_2 window for in situ FTIR. The electrode-covered catalysts were first electrochemically activated by cyclic voltammetry for several cycles in N_2-saturated 1 M KOH. After that, multi-stepped FTIR spectroscopy (MS-FTIR) was utilized to collect spectra in 1 M KOH 1 M C_2H_5OH electrolyte from 0.2 to 1.2 V (vs RHE) at 0.1 V intervals. The relative change in reflectivity ($\Delta R/R$) of spectra was calculated by the following equation:

$$\frac{\Delta R}{R} = \frac{R(E_S) - R(E_R)}{R(E_R)} \quad (2)$$

$R(E_S)$ represented the catalyst's potential E_S, and E_R was the reference potential. The reference potential was at –0.857 V (vs SCE).

Electrochemical Measurements: All electrochemical measurements for the EOR and HER tests were performed at 298 K by employing a three-electrode electrochemical cell with an electrochemical workstation (CHI, 760E).

HER Measurements: Before the HER measurement, all catalyst inks were obtained by ultrasonic catalysts (2 mg) dispersed in isopropanol (1 mL) for 30 min. Then, the catalyst ink was deposited on carbon paper (1 × 1 cm^2), and then 20 µL of Nafion solution (5 wt.%, Sigma–Aldrich) was covered. The carbon paper was used as the working electrode with a graphite rod-counter electrode and a saturated calomel electrode (SCE)-reference electrode. The double-layer capacitances (C_{dL}) were determined by recording the CV curves at scan rates from 10 to 50 mV s^{-1} at 5 mV intervals. The HER performance was estimated by linear sweep voltammetry (LSV) to gain the polarization curves at a sweep rate of 5 mV s^{-1}. The long-term stability tests of the HER were realized by measuring CV curves of 5000 and 20 000 circles at a sweep rate of 50 mV s^{-1}. The electrochemical impedance spectroscopy (EIS) was determined at the open-circuit voltage in the frequency range of 0.1–100 000 Hz.

EOR Measurements: All catalyst inks were prepared by ultrasonic catalysts (2 mg) dispersed in isopropanol (1 mL) for 30 min. Then, the 10 µL catalyst ink was deposited on a glassy carbon electrode and then 5 µL of Nafion solution (0.25 wt.%, Sigma–Aldrich) was dropwise added. After desiccation, the working electrode was activated by combining with the counter electrode (Pt foil) and the reference electrode (saturated calomel electrode, SCE) by cyclic voltammetry in the N_2-saturated 1 M KOH for 50 cycles. The EOR curves were collected by cyclic voltammetry with a sweep rate of 50 mV s^{-1} in the N_2-saturated 1 M KOH + 1 M C_2H_5OH. The chronoamperometry was conducted at 0.757 V (vs RHE) for 4000 s to evaluate the EOR stability.

CO-Stripping Measurements: The CO-saturated 1 M KOH solution was gained by bubbling with 20% CO/N_2 gas for 15 min. Then, the chronoamperometry at –0.96 V in 1 M KOH for 1 h was adopted to achieve the monolayer of CO adsorbed on the sample. After that, the 1 M KOH solution without the adsorbed CO was obtained by blowing N_2 gas for 0.5 h. CO-stripping measurements were conducted by cyclic voltammetry for two cycles at 0–1.25 V (vs RHE). The electrochemical active surface area (ECSA) of all those catalysts was calculated, based on the peak areas of their CO-stripping experiments and the equation of $ECSA = Q/(M_{Pd} \cdot C_{Pd})$, where Q was the charge of the CO-stripping peak, M was the mass of Pd dropped on a glassy carbon electrode, C was the capacitance value of Pd (420 µC cm^{-2}).

Supporting Information

Supporting Information is available from the Wiley Online Library or from the author.

Acknowledgements

A.P., G.L., and L.Z. contributed equally to this work. This work was supported by the National Natural Science Foundation of China (Grant No. 22162012 and 22202089), Youth Jinggang Scholars Program in Jiangxi Province ([2019]57), the Thousand Talents Plan of Jiangxi Province (jxsq2019201083), Program of Qingjiang Excellent Young Talents, Jiangxi University of Science and Technology (JXUSTQJBJ2019002), Foundation of State Key Laboratory of Coal Conversion (Grant No. J22-23-609), Jiangxi Provincial Key Laboratory of Functional Molecular Materials Chemistry (20212BCD42018), Program of Technology Innovation Talents of Ganzhou, Research Fund Program of Guangdong Provincial Key Lab of Green Chemical Product Technology (GC202102), Research Fund Program of Key Laboratory of Fuel Cell Technology of Guangdong Province and HK Scholars Program. This project was funded by the Researcher Supporting Project Number (RSP-2021/405), King Saud University, Riyadh, Saudi Arabia. This publication has been supported by RUDN University Strategic Academic Leadership Program (R.L.). R.L. gratefully acknowledges funding for Open Access to Universidad de Cordoba/CBUA.

Conflict of Interest

The authors declare no conflict of interest.

Data Availability Statement

The data that support the findings of this study are available in the supplementary material of this article.

Keywords

electrocatalyses, ethanol oxidation reactions, hydrogen evolution reactions, palladium nanoclusters, Pt-free electrocatalysts, ruthenium single atoms

Received: August 2, 2022
Revised: August 31, 2022
Published online: October 17, 2022

[1] J. Goldemberg, *Science* **2007**, *315*, 808.
[2] L. Shang, Y. Zhao, X. Y. Kong, R. Shi, G. I. Waterhouse, L. Wen, T. Zhang, *Nano Energy* **2020**, *78*, 105375.
[3] M. Li, Z. Xia, M. Luo, L. He, L. Tao, W. Yang, Y. Yu, S. Guo, *Small Sci.* **2021**, *1*, 2100061.
[4] X. Liu, R. Guo, K. Ni, F. Xia, C. Niu, B. Wen, J. Meng, P. Wu, J. Wu, X. Wu, L. Mai, *Adv. Mater.* **2020**, *32*, 2001136.
[5] H. Dotan, A. Landman, S. W. Sheehan, K. D. Malviya, G. E. Shter, D. A. Grave, Z. Arzi, N. Yehudai, M. Halabi, N. Gal, N. Hadari, C. Cohen, A. Rothschild, G. S. Grader, *Nat. Energy* **2019**, *4*, 786.
[6] G. Ren, J. Liu, J. Wan, Y. Guo, D. Yu, *Appl. Energy* **2017**, *204*, 47.
[7] S. Sharma, S. K. Ghoshal, *Renew. Sust. Energy Rev.* **2015**, *43*, 1151.
[8] R. A. Walters, M. R. Tarbotton, C. E. Hiles, *Renew. Energy* **2013**, *51*, 255.
[9] T. M. Gür, *Energy Environ. Sci.* **2018**, *11*, 2696.
[10] S. Kélouwani, K. Agbossou, R. Chahine, *J. Power Sources* **2005**, *140*, 392.
[11] C. Baeumer, J. Li, Q. Lu, A. Y. L. Liang, L. Jin, H. P. Martins, T. Duchoň, M. Glöß, S. M. Gericke, M. A. Wohlgemuth, M. Giesen, E. E. Penn, R. Dittmann, F. Gunkel, R. Waser, M. Bajdich, S. Nemšák, J. T. Mefford, W. C. Chueh, *Nat. Mater.* **2021**, *20*, 674.
[12] J. Zhang, T. Wang, P. Liu, Z. Liao, S. Liu, X. Zhuang, M. Chen, E. Zschech, X. Feng, *Nat. Commun.* **2017**, *8*, 1.
[13] S. Li, J. Wang, X. Lin, G. Xie, Y. Huang, X. Liu, H. J. Qiu, *Adv. Funct. Mater.* **2021**, *31*, 2007129.
[14] S. Shen, T. S. Zhao, J. Xu, Y. Li, *Energy Environ. Sci.* **2011**, *4*, 1428.
[15] C. Liu, Y. Shen, J. Zhang, G. Li, X. Zheng, X. Han, L. Xu, S. Zhu, Y. Chen, Y. Deng, W. Hu, *Adv. Energy Mater.* **2022**, *12*, 2103505.
[16] J. Guo, R. Chen, F. C. Zhu, S. G. Sun, H. M. Villullas, *Appl. Catal., B* **2018**, *224*, 602.
[17] L. An, T. S. Zhao, *Energy Environ. Sci.* **2011**, *4*, 2213.
[18] I. Ledezma-Yanez, W. D. Z. Wallace, P. Sebastián-Pascual, V. Climent, J. M. Feliu, M. T. Koper, *Nat. Energy* **2017**, *2*, 17031.
[19] S. H. Han, H. M. Liu, P. Chen, J. X. Jiang, Y. Chen, *Adv. Energy Mater.* **2018**, *8*, 1801326.

[20] M. K. Debe, *Nature* **2012**, *486*, 43.
[21] X. Qin, L. Zhang, G. L. Xu, S. Zhu, Q. Wang, M. Gu, X. Zhang, C. Sun, P. B. Balbuena, K. Amine, M. Shao, *ACS Catal.* **2019**, *9*, 9614.
[22] I. T. McCrum, M. T. Koper, *Nat. Energy* **2020**, *5*, 891.
[23] Y. Liu, X. Li, Q. Zhang, W. Li, Y. Xie, H. Liu, L. Shang, Z. Liu, Z. Chen, L. Gu, Z. Tang, T. Zhang, S. Lu, *Angew. Chem., Int. Ed.* **2020**, *59*, 1718.
[24] R. Subbaraman, D. Tripkovic, D. Strmcnik, K. C. Chang, M. Uchimura, A. P. Paulikas, V. Stamenkovic, N. M. Markovic, *Science* **2011**, *334*, 1256.
[25] Z. Xing, C. Han, D. Wang, Q. Li, X. Yang, *ACS Catal.* **2017**, *7*, 7131.
[26] R. Subbaraman, D. Tripkovic, K. C. Chang, D. Strmcnik, A. P. Paulikas, P. Hirunsit, M. Chan, J. Greeley, V. Stamenkovic, N. M. Markovic, *Nat. Mater.* **2012**, *11*, 550.
[27] W. Huang, H. Wang, J. Zhou, J. Wang, P. N. Duchesne, D. Muir, P. Zhang, N. Han, F. Zhao, M. Zeng, J. Zhong, C. Jin, Y. Li, S. T. Lee, H. Dai, *Nat. Commun.* **2015**, *6*, 1.
[28] S. Sinthika, S. T. Vala, Y. Kawazoe, R. Thapa, *ACS Appl. Mater. Interfaces* **2016**, *8*, 5290.
[29] S. Li, J. Shu, S. Ma, H. Yang, J. Jin, X. Zhang, R. Jin, *Appl. Catal., B* **2021**, *280*, 119464.
[30] F. Lv, W. Zhang, M. Sun, F. Lin, T. Wu, P. Zhou, W. Yang, P. Gao, B. Huang, S. Guo, *Adv. Energy Mater.* **2021**, *11*, 2100187.
[31] G. R. Xu, Y. N. Zhai, F. M. Li, G. T. Zhao, S. N. Li, H. C. Yao, J. X. Jiang, Y. Chen, *Nanoscale* **2019**, *11*, 13477.
[32] C. Hu, L. Zhang, J. Gong, *Energy Environ. Sci.* **2019**, *12*, 2620.
[33] Z. Luo, J. Li, Y. Li, D. Wu, L. Zhang, X. Ren, C. He, Q. Zhang, M. Gu, X. Sun, *Adv. Energy Mater.* **2022**, *12*, 2103823.
[34] S. Guo, S. Dong, E. Wang, *Energy Environ. Sci.* **2010**, *3*, 1307.
[35] F. Gao, Y. Zhang, F. Ren, Y. Shiraishi, Y. Du, *Adv. Funct. Mater.* **2020**, *30*, 2000255.
[36] S. Zhang, A. Pei, G. Li, L. Zhu, G. Li, F. Wu, S. Lin, W. Chen, B. H. Chen, R. Luque, *Green Chem.* **2022**, *24*, 2438.
[37] L. Zhu, Y. Sun, H. Zhu, G. Chai, Z. Yang, C. Shang, H. Ye, B. H. Chen, A. Kroner, Z. X. Guo, *ACS Catal.* **2022**, *12*, 8104.
[38] C. Du, H. Huang, Y. Wu, S. Wu, W. Song, *Nanoscale* **2016**, *8*, 16251.
[39] F. T. Tsai, Y. T. Deng, C. W. Pao, J. L. Chen, J. F. Lee, K. T. Lai, W. F. Liaw, *J. Mater. Chem., A* **2020**, *8*, 9939.
[40] T. Wu, J. Fan, Q. Li, P. Shi, Q. Xu, Y. Min, *Adv. Energy Mater.* **2018**, *8*, 1701799.
[41] Y. J. Shih, Y. H. Huang, C. P. Huang, *Electrochim. Acta* **2018**, *263*, 261.
[42] O. Diaz-Morales, D. Ferrus-Suspedra, M. T. Koper, *Chem. Sci.* **2016**, *7*, 2639.
[43] A. Kowal, M. Li, M. Shao, K. Sasaki, M. Vukmirovic, J. H. Zhang, N. Marinkovic, P. Liu, A. Frenkel, R. Adzic, *ACS Catal.* **2016**, *6*, 4894.
[44] M. C. Figueiredo, R. M. Arán-Ais, J. M. Feliu, K. Kontturi, T. Kallio, *J. Catal.* **2014**, *312*, 78.
[45] N. Erini, V. Beermann, M. Gocyla, M. Gliech, M. Heggen, R. E. Dunin-Borkowski, P. Strasser, *Angew. Chem., Int. Ed.* **2017**, *129*, 6633.
[46] J. E. Sulaiman, S. Zhu, Z. Xing, Q. Chang, M. Shao, *ACS Catal.* **2017**, *7*, 5134.
[47] F. Zhao, J. Ye, Q. Yuan, X. Yang, Z. Zhou, *J. Mater. Chem., A* **2020**, *8*, 11564.
[48] Z. Chen, J. Zhang, Y. Zhang, Y. Liu, X. Han, C. Zhong, W. Hu, Y. Deng, *Nano Energy* **2017**, *42*, 353.
[49] Y. H. Wang, X. T. Wang, H. Ze, X. G. Zhang, P. M. Radjenovic, Y. J. Zhang, J. C. Dong, Z. Q. Tian, J. F. Li, *Angew. Chem., Int. Ed.* **2021**, *133*, 5772.
[50] E. J. Lim, Y. Kim, S. M. Choi, S. Lee, Y. Noh, W. B. Kim, *J. Mater. Chem., A* **2015**, *3*, 5491.
[51] L. Zhu, H. Zhang, N. Ma, C. Yu, N. Ding, J. L. Chen, C.-W. Pao, J.-F. Lee, Q. Xiao, B. H. Chen, *J. Catal.* **2019**, *377*, 299.
[52] L. Zhu, H. Zhu, M. Shakouri, L. Zeng, Z. Yang, Y. Hu, H. Ye, H. Wang, B. H. Chen, R. Luque, *Appl. Catal., B* **2021**, *297*, 120404.
[53] B. Ravel, M. Newville, *J. Synchrotron Radiat.* **2005**, *12*, 537.